ARTICLE OPEN

Greatly enhanced tunneling electroresistance in ferroelectric tunnel junctions with a double barrier design

Wei Xiao [1,2], Xiaohong Zheng [3✉], Hua Hao[4], Lili Kang[5], Lei Zhang [6,7✉] and Zhi Zeng [1,2]

We propose that the double barrier effect is expected to enhance the tunneling electroresistance (TER) in the ferroelectric tunnel junctions (FTJs). To demonstrate the feasibility of this mechanism, we design a model structure of Pt/BaTiO$_3$/LaAlO$_3$/Pt/BaTiO$_3$/LaAlO$_3$/Pt double barrier ferroelectric tunnel junction (DB-FTJ), which can be considered as two identical Pt/BaTiO$_3$/LaAlO$_3$/Pt single barrier ferroelectric tunnel junctions (SB-FTJs) connected in series. Based on density functional calculation, we obtain the giant TER ratio of 2.210×10^8% in the DB-FTJ, which is at least three orders of magnitude larger than that of the SB-FTJs of Pt/BaTiO$_3$/LaAlO$_3$/Pt, together with an ultra-low resistance area product (0.093 K$\Omega\mu$m^2) in the high conductance state of the DB-FTJ. Moreover, it is possible to control the direction of polarization of the two single ferroelectric barriers separately and thus four resistance states can be achieved, making DB-FTJs promising as multi-state memory devices.

npj Computational Materials (2023)9:144 ; https://doi.org/10.1038/s41524-023-01101-9

INTRODUCTION

Ferroelectric tunnel junctions (FTJs) have been studied quite extensively since nanoscale ferroelectricity were demonstrated in thin films[1–3]. The intensive research interest stems from the great potential of FTJs as important candidates for non-volatile memory[4–12]. A FTJ is usually a sandwich structure (metal/ferroelectric/metal or M/F/M)[5,13–24] and is characterized by the tunneling electroresistance (TER), which measures the difference in conductance between the two ferroelectric polarization states. Another kind of FTJs which include an interlayer (I) at the F/M interface (M/F/I/M) have also been proposed to achieve substantially improved performance of FTJs[25–34]. For a FTJ, a large TER ratio is essential to distinguish between different resistance states and thus plays a central role in the practical application of the FTJs. Thus far, various mechanisms or strategies have been proposed to achieve a large TER, such as using domain wall states[21,22], the screening effect of electrodes[5,15], defects[20], phase transitions[30], polar interfaces[33], and interfacial large polarization[34], etc.

For electrons tunneling through a single barrier (SB), the tunneling probability decreases exponentially with the barrier width and height[35]. This property has been widely utilized in the design of the SB-FTJs. As a matter of fact, in the study of the TER effect of the SB-FTJs, almost all the present proposed methods are related to the modulation of the effective barrier width or/and barrier height. In contrast to single barrier structures, double-barrier structures, consisting of two tunneling barriers or scatterers a and b in series with individual transmission probability T_a and T_b, respectively, are another kind of well-investigated objects in mesoscopic transport theory[36]. Double-barrier structures present interesting transport behaviors, such as resonant tunneling and single electron tunneling, which are absent in single barrier structures. Particularly, the overall transmission probability T' of double barrier structures is related to both T_a and T_b, in a certain form $T' = f(T_a, T_b)$, depending on the actual working regime. When applied in the design of the FTJs, the FTJs with double barriers may show much larger difference between the T'_1 in the high conductance state and T'_2 in the low conductance state as compared with single barrier FTJs and subsequently greatly enhanced TER ratio.

In order to clarify this, we start with an ideal case where $f(T_a, T_b) = T_a T_b$, which means a sequential tunneling process, with the electrons tunneling through the two barriers sequentially[37] and independently, and suppose the ON/OFF ratio for each barrier is $n_a = T_{a1}/T_{a2}$ and $n_b = T_{b1}/T_{b2}$, then for the DB-FTJs, we will have $n_{db} = n_a n_b$. For a double barrier consisting of two identical single barriers with equal transmission probability $T_{a1} = T_{b1} = T_1$ and $T_{a2} = T_{b2} = T_2$, the overall transmission probability for the DB-FTJ will be $T'_1 = T_1^2$ and $T'_2 = T_2^2$. Thus we will have $n_{db} = T'_1/T'_2 = (T_1/T_2)^2$, which means that the ON/OFF ratio (T'_1/T'_2) for the DB-FTJs will increase quadratically with that (T_1/T_2) of the SB-FTJs as shown in Fig. 1a and thus is much larger than that of the SB-FTJs when $T_1/T_2 > 1$ which actually always holds. The same prediction can be drawn from more accurate theoretical formulae, as discussed below. In the incoherent resonant tunneling regime, we have $T'_1 = T_1^2/(1 - R_1^2)$ and $T'_2 = T_2^2/(1 - R_2^2)$[36], where R_1 and R_2 represent the reflection probabilities corresponding to the two transmission probabilities T_1 and T_2 of the SB-FTJs. It is seen that the ON/OFF ratio T'_1/T'_2 for the DB-FTJs is still much larger than that of the SB-FTJs [see Fig. 1b]. If we further take the phase shift θ between the two scatterers into account, namely, in the coherent resonant tunneling, we will have $T'_1 = T_1^2/(1 - 2R_1 \cos\theta + R_1^2), T'_2 = T_2^2/(1 - 2R_2 \cos\theta + R_2^2)$[36]. It is seen that in a very wide range of $\cos\theta$, T'_1/T'_2 is much larger than T_1/T_2 and only when $\cos\theta$ is very close to 1 will the ON/OFF ratio be close to 1 [see Fig. 1c], which means that the ON/OFF ratio will be greatly increased in most cases by changing from SB to DB in the design of the FTJs. Thus, no matter whether the DB-FTJ is in coherent tunneling regime or incoherent tunneling regime, the double barrier structure may lead to the great increase of the TER ratio in

[1]Key Laboratory of Materials Physics, Institute of Solid State Physics, HFIPS, Chinese Academy of Sciences, Hefei 230031, China. [2]Science Island Branch of Graduate School, University of Science and Technology of China, Hefei 230026, China. [3]College of Information Science and Technology, Nanjing Forestry University, Nanjing 210037, China. [4]School of Physics, Hangzhou Normal University, Hangzhou 311121, China. [5]Institute for Computational Materials Science, School of Physics and Electronics, Henan University, Kaifeng 475004, China. [6]State Key Laboratory of Quantum Optics and Quantum Optics Devices, Institute of Laser Spectroscopy, Shanxi University, Taiyuan 030006, China. [7]Collaborative Innovation Center of Extreme Optics, Shanxi University, Taiyuan 030006, China. ✉email: xhzheng@njfu.edu.cn; zhanglei@sxu.edu.cn
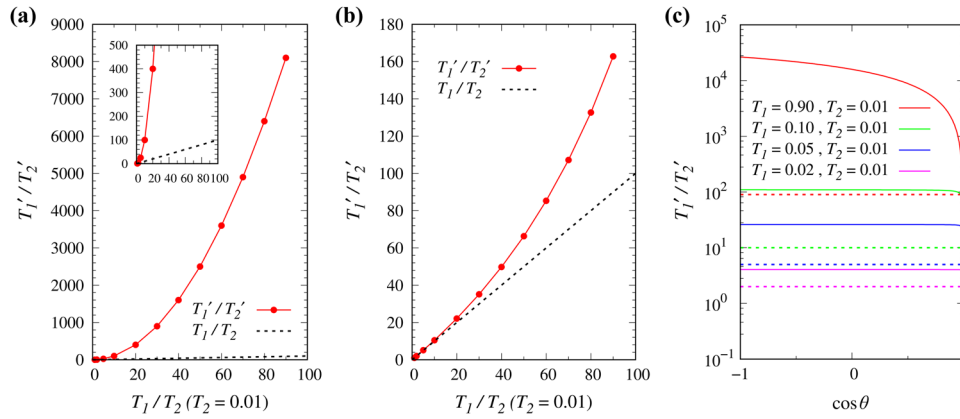
Fig. 1 Comparison of ON/OFF ratio prediction between SB-FTJs and DB-FTJs. The relationship between the ON/OFF ratio of the DB-FTJs (T_1'/T_2', solid line) and that of the SB-FTJs (T_1/T_2, dashed line) when the DB-FTJs work in a regime of: **a** an ideal sequential tunneling, but with the electrons tunneling through the two barriers independently; **b** incoherent tunneling; **c** coherent tunneling. Since it is just for a trend prediction, we assume $T_1 = 0.01$ and increase T_2 to see how T_1'/T_2' changes with T_1/T_2. In (**c**), the solid line curve and the dashed line curve with the same color show the value of T_1'/T_2' and T_1/T_2, respectively, as a function of $\cos\theta$ with the same T_1 and T_2. It is seen that the position of the solid line is much higher than that of the dashed line, suggesting much increased ON/OFF ratio.

comparison with the SB-FTJs. These preliminary estimations suggest a proposal for achieving greatly enhanced TER by designing DB-FTJs which have two identical ferroelectric barriers in series between the two electrodes.

To verify the feasibility of this proposal, we construct and study a DB-FTJ with the Pt/BaTiO$_3$/LaAlO$_3$/Pt/BaTiO$_3$/LaAlO$_3$/Pt structure where each single barrier BaTiO$_3$/LaAlO$_3$ (BTO/LAO) consists of 5.5 unit cell (u.c.) BTO and 1 u.c. LAO, with a nanometer-thick Pt film separating them. Based on density functional calculations, we obtain a significant enhancement of TER ratio in the DB-FTJ compared with the SB-FTJ [the Pt/BTO (5.5 u.c.)/LAO (1 u.c.)/Pt FTJ or the Pt/BTO (11.5 u.c.)/LAO (1 u.c.)/Pt FTJ]. Moreover, the double barrier design shows other great advantages over single barrier design, such as ultra-low resistance area product (RA) in the high conductance state and versatility for realizing multiple state storage with free control by gate voltage.

RESULTS AND DISCUSSION
DB-FTJ

Figure 2a shows the relaxed structures of the two polarization states of the DB-FTJ, in which the ferroelectric polarization directions of the two single barriers both point to left or right. The energy switching barrier between the left and right polarization states is obtained by linear interpolation of atomic coordinates ($z(\delta) = (1 - \delta)z(P_{\leftarrow}) + \delta z(P_{\rightarrow})$), which proves the bistable property of the DB-FTJ [Fig. 3]. It is worth noting that the positively charged (LaO)$^+$ plane of polar oxide LaAlO$_3$ repels Ti$^+$ ions at the BTO/LAO interface, resulting in abnormal polarization in the rightmost region of each single ferroelectric barrier BTO in the right polarization state, which can be seen more clearly from the Ti-O displacement of the BTO in Fig. 2b. However, for the left polarization state of the DB-FTJ, the two single ferroelectric barriers BTO are almost uniformly polarized. The electrostatic potential energy distributions of the two polarization states of the DB-FTJ are shown in Fig. 2c. It is seen that the electrostatic potential energy of the right polarization state is higher than that of the left polarization state for the left half region of each single barrier, while the situation is opposite for the right half region of each single barrier. This can be understood as follows. Generally, the electron potential energy decreases along the polarization direction. Thus we see that the overall potential energy decreases in both single barriers in the right polarized state and increases in the left polarized state from left to right. However, due to the positively charged (LaO)$^+$ plane at the right interface of each

single barrier, the electron potential energy will be decreased by it due to the Coulomb attractive interaction from it. That is why we see a drop after a long increase in the left polarized state and further decrease after a long decrease in the right polarized state at the right interface, leading to different maximum positions in each single barrier. The shape of the barrier has an important relationship with the transmission of electrons, therefore, the transport characteristics of the two polarization states of the DB-FTJ are studied next.

The $\mathbf{k}_\parallel$-resolved transmissions in the two-dimensional Brillouin zone (2DBZ) at the Fermi energy are calculated for the two polarization states of the DB-FTJ and presented in Fig. 2d. The high transmission of the right polarization state appears as a bright red cross shape in the 2DBZ, with higher transmission especially near the $\bar{\Gamma}$ point. However, for the left polarization state, almost the whole 2DBZ exhibits low transmission. The equilibrium conductance for the left polarization state is integrated as $9.978 \times 10^{-12}(2e^2h^{-1})$ and that for the right polarization state as $2.205 \times 10^{-5}(2e^2h^{-1})$, where e and h are electron charge and Plank's constant, respectively. The TER ratio is subsequently obtained as $2.210 \times 10^8\%$, which is at least three orders of magnitude larger than that of the SB-FTJs to be shown later. Moreover, we find that the RA obtained is ultra low (0.093 K$\Omega\mu$m^2) in the high conductance state of the DB-FTJ, which enables this state to be easily detected and greatly increases the compatibility of the FTJs with the present complementary metal-oxide semiconductor (CMOS) electronics.

To reveal the origin for the large TER ratio and ultra-low RA of the DB-FTJ, we draw the projected density of states (PDOS) distribution as shown in Fig. 4a. In the right polarization state, since the positive ferroelectric bound charges and the positively charged (LaO)$^+$ plane of the right interface region of each single barrier together lead to a low electrostatic potential energy distribution in this region [Fig. 2c, red line], the conduction band minimum (CBM) in this region drops below the Fermi energy [Fig. 4a, bottom panel], which effectively reduces the width of each single barrier and increases the transmission. This leads to a high conductance state, and correspondingly, the RA decreases. However, for the left polarization state, the electrostatic potential energy distribution increases due to the neutralization of the negative ferroelectric bound charges and the positive (LaO)$^+$ plane in the right interface region of each single barrier [Fig. 2c, blue line], thus placing the Fermi energy almost entirely in the band gap [Fig. 4a, top panel]. We notice that the Fermi energy crosses the density of states of the d_{xy} orbitals near the left interface of each single barrier in the left polarization state, and
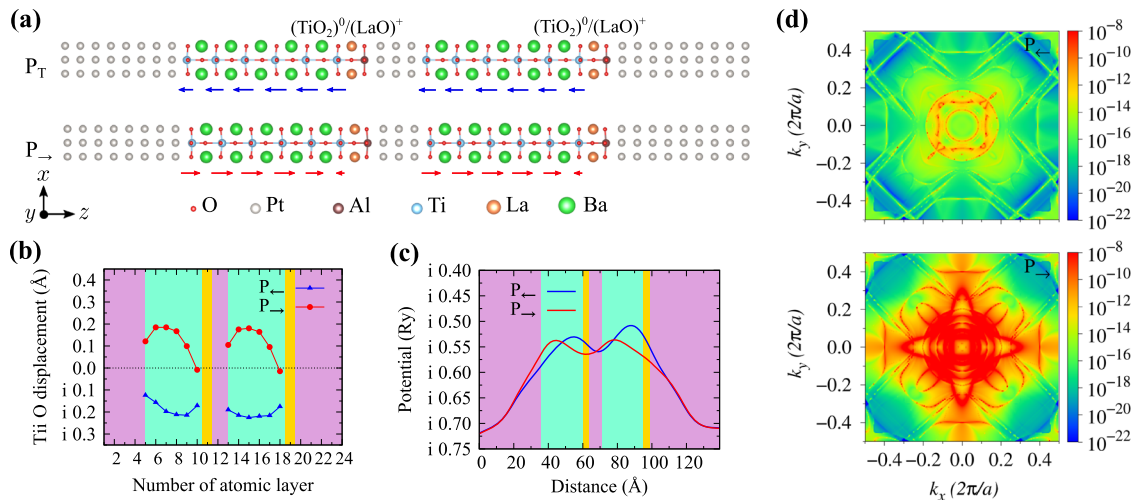
Fig. 2 Atomic structure, electronic structure and transport properties of the DB-FTJ. a Relaxed atomic structures of the two polarization states of the DB-FTJ, with the direction and magnitude of local polarization of the BTO indicated by the arrows below the structure. **b** The Ti-O displacement of each layer of TiO_2 plane in BTO along the z-direction. **c** The average electrostatic potential energy of left and right polarization states along z-direction. The pink, cyan, and yellow backgrounds in (**b**) and (**c**) represent Pt, BTO, and LAO, respectively. **d** The $k_\parallel$-resolved transmission of the 2DBZ of left and right polarization states of the DB-FTJ at Fermi energy.
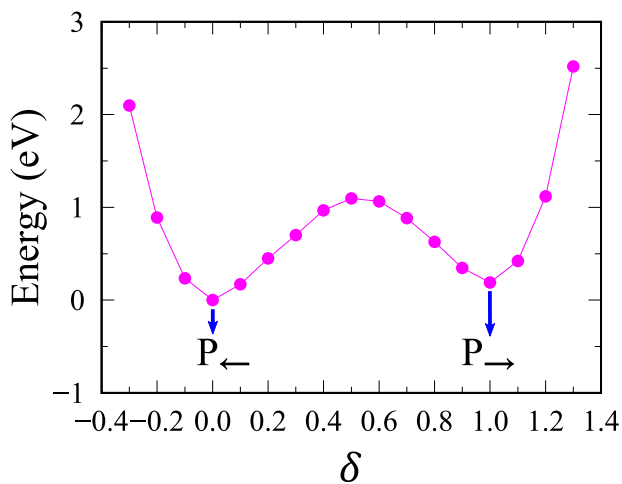

Fig. 3 Energy switch barrier between the left and right polarization states of the DB-FTJ. $P_\leftarrow$ ($\delta = 0.0$) and $P_\rightarrow$ ($\delta = 1.0$) represent the left and right polarization states, respectively. The value of δ changes from -0.3 to $+1.3$.

these local density of states will produce resonance tunneling effects to contribute to the conductance of this polarization state. However, by calculating the orbital resolved density of the scattering states, we find that the conductance contribution of the resonant tunneling effect generated by this local state is small compared with the conductance contribution generated by its neighboring d_{yz} orbital (as well as the d_{z^2} and d_{xz} orbitals) above the Fermi energy [the second layer in Supplementary Fig. 1]. This is due to the fact that the d_{xy} orbitals are localized in the xy plane and the d_{yz} (as well as the d_{z^2} and d_{xz} orbitals) orbitals are along the transport z direction. Therefore, the conductance enhancement effect of the d_{xy} orbitals near the left interface in this polarization state is quite weak, which is exactly consistent with the low transmission coefficient value $9.978 \times 10^{-12} (2e^2h^{-1})$ in this polarization state. Consequently, the left polarization state is a low conductance state compared to the right polarization state. The fact that Fermi energy passes finite density of states in several layers in the right interface region of each single barrier in the right polarization state of the DB-FTJ can also be seen from the distribution of real space charge density in Fig. 4, that

is, the accumulation of charge density in the right polarization state shown in the black dashed box in Fig. 4b. Further analysis shows that the density of states near Ti atoms in the black dotted box in Fig. 4b mainly comes from the d_{yz} and d_{xz} orbitals of Ti atoms [Fig. 4c]. Therefore, these orbitals along the transport z-direction play a crucial role in the high conductance state of the right polarization state of the DB-FTJ. However, the small charge density near the left interface of each single barrier in the left polarization state of Fig. 4b mainly comes from the local d_{xy} orbitals of the Ti atoms [Fig. 4b] with weak conductance contribution [the second layer in Supplementary Fig. 1]. Due to the underestimation of the band gap by density functional theory (DFT), we also considered DFT+U by setting the U value to 5 eV or 8 eV in the d orbital of Ti. Interestingly, the metallization at the right interface in the right polarization state still exists [Supplementary Fig. 2], so the double barrier effect will still be valid.

In order to obtain more information about the electronic structure of the DB-FTJ, we calculate the orbital resolved and $k_\parallel$-resolved density of states of the Ti atom and Pt atom at the Fermi energy in the blue dotted circles in Fig. 4b. Since the s orbitals of these atoms have almost no density of states at the Fermi energy [the five layer in Fig. 4c and the Supplementary Fig. 3], we only list the $k_\parallel$-resolved density of states of the d orbitals of these atoms. As can be seen from Fig. 5a, the d_{xy}, d_{yz} and d_{xz} orbitals of the Ti atom show a higher density of states at some k points in the 2DBZ, while the d_{z^2} and $d_{x^2-y^2}$ orbitals show a lower density of states in the whole 2DBZ, which is obviously consistent with the layer resolved density of states in the five layer in Fig. 4c. It is proved that the high conductance of the right polarization state is mainly contributed by the d_{yz} and d_{xz} orbitals, and as we have analyzed before, the resonant tunneling effect of the local d_{xy} orbitals will make a weak contribution to the conductance of this polarization state. For the Pt atom in Fig. 5b, each d orbital shows a higher density of states in the 2DBZ, which is also consistent with the layered resolved density of states of the Pt atom [Supplementary Fig. 3], indicating the metallic characteristics of the Pt electrode. In addition, we note that the density of states of these orbitals has different shapes in the 2DBZ, and we argue that these shapes are related to the coordination environment around the atoms, which is worthy for further study.
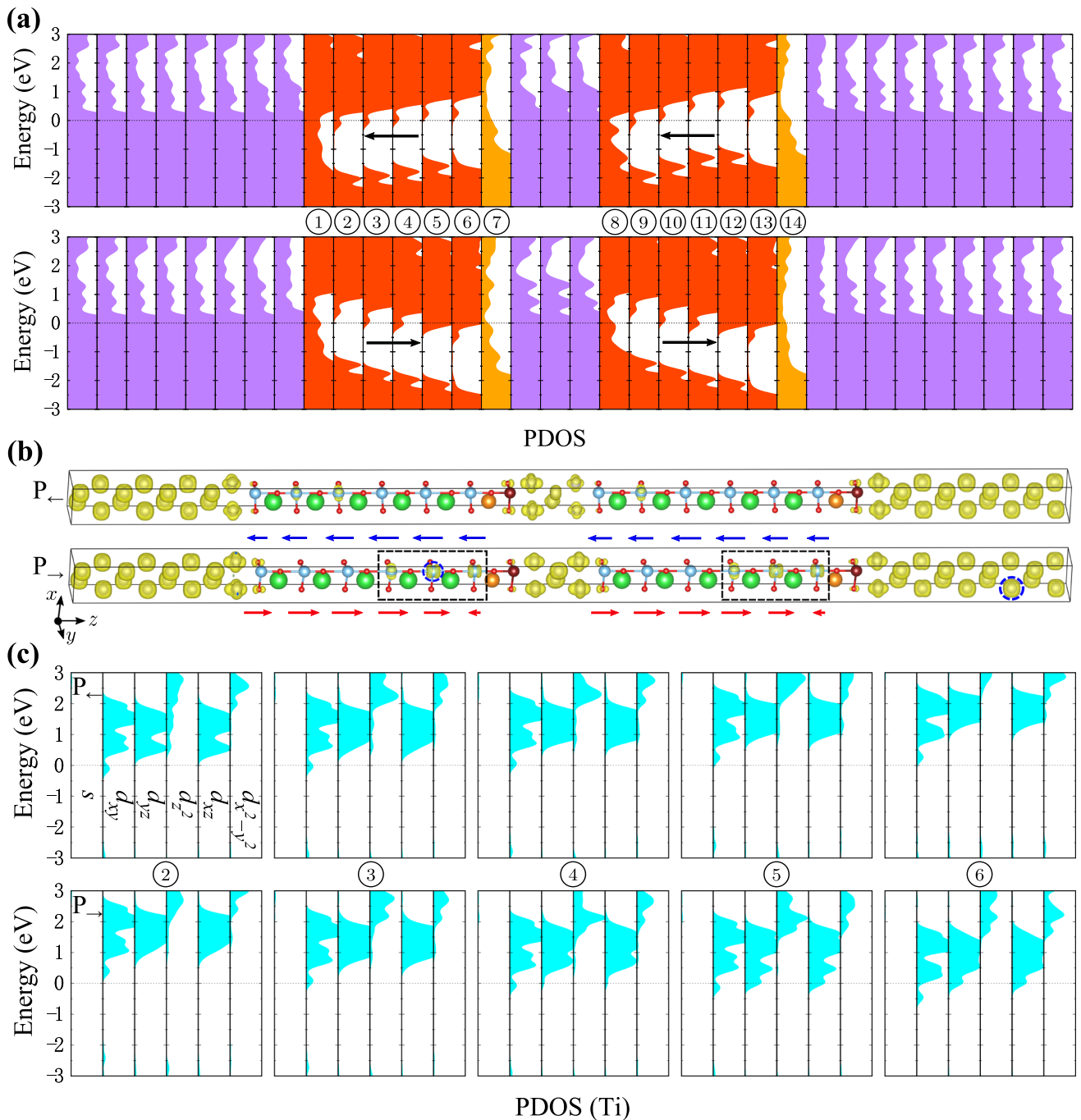
(a)

PDOS

(b)

(c)

PDOS (Ti)

Fig. 4 Layer resolved and orbital resolved density of states and charge density analysis of the DB-FTJ. a The layer resolved density of states distribution of Pt electrode (purple), TiO_2 layer (red), AlO_2 layer (golden yellow). The black arrows indicate the polarization directions. The number in the circle marks the corresponding atomic layer. **b** Real space partial charge density distribution (Visualized with VESTA code[47], with the isovalues set to 0.003). The blue and red arrows below indicate the local polarization of the two polarization states. The atoms in the blue dotted circles are selected for further orbital and $\mathbf{k}_\parallel$-resolved DOS analysis. **c** The orbital resolved density of states distribution of Ti atoms in layers 2 to 6.

SB-FTJs

For comparison, we have also studied the transport properties of two SB-FTJs with different ferroelectric barriers (BTO) thicknesses. From this study, we will see directly whether single barrier works as well or even better so that doube barrier design is unnecessary or not. The first SB-FTJ has a BTO thickness of 5.5 u.c., which is the same as that of the single barrier in the DB-FTJ. The relaxed structures of the two polarization states are shown in Fig. 6a. The polarization of the ferroelectric barrier BTO in the SB-FTJ is similar

to that of each single barrier in the DB-FTJ, as can be seen from the local polarization arrows marked at the bottom of each structure and the Ti-O displacement of the ferroelectric barrier BTO [see Supplementary Fig. 4a in the supplemental material]. As expected, this similarity also shows up in the electrostatic potential energy distribution [see Supplementary Fig. 4b] and the projected density of states distribution [see Supplementary Fig. 5]. The $\mathbf{k}_\parallel$-resolved transmissions at the Fermi energy for the two polarization states are shown in Fig. 6b, which clearly shows
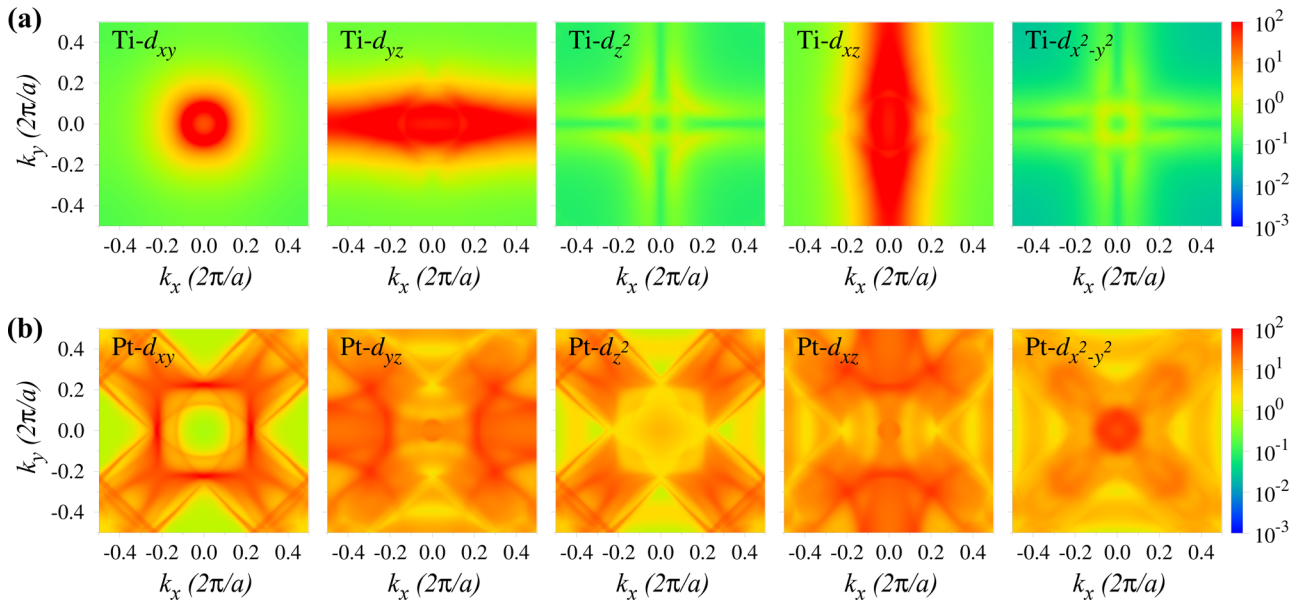
Fig. 5 Orbital resolved and k∥-resolved DOS analysis of the DB-FTJ. The orbital resolved and k∥-resolved DOS of Ti atom (**a**) and Pt atom (**b**) in the blue dotted circle in the right polarization state of the DB-FTJ of Fig. 4b.
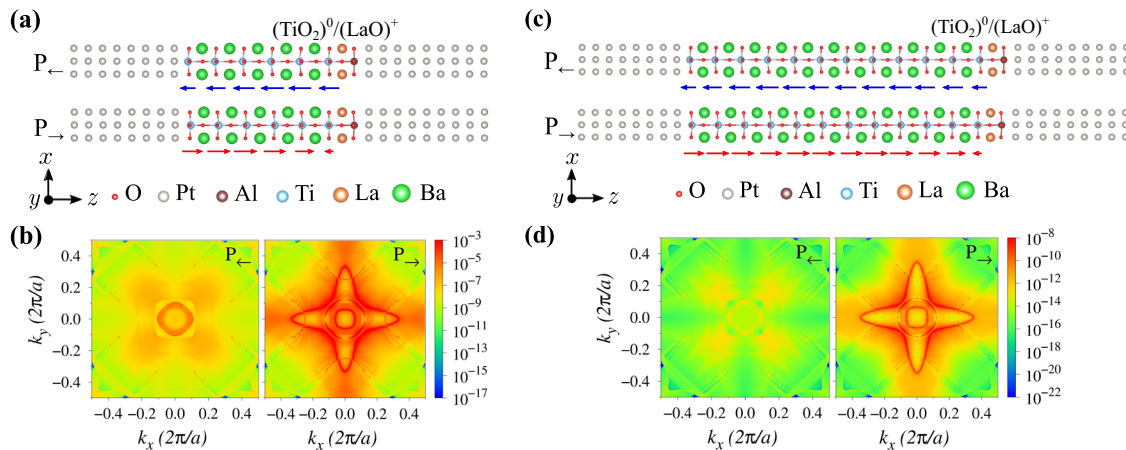

Fig. 6 Atomic structure and transport properties of SB-FTJs. a Relaxed atomic structures and local polarizations of the SB-FTJ with BTO thickness of 5.5 u.c. **b** The k∥-resolved transmission of the 2DBZ of left and right polarization states of the system at Fermi energy. **c** Relaxed atomic structures and local polarizations of the SB-FTJ with BTO thickness of 11.5 u.c. **d** The k∥-resolved transmission of the 2DBZ of left and right polarization states of the system at Fermi energy.

that the right polarization state conducts much better than the left polarization state. This can be seen more quantitatively by the equilbrium conductances $G_\rightarrow = 7.301 \times 10^{-5}(2e^2h^{-1})$ and $G_\leftarrow = 1.373 \times 10^{-7}(2e^2h^{-1})$, which gives rise to a TER ratio of $5.306 \times 10^4\%$, about four orders of magnitude smaller than that of the DB-FTJ. Furthermore, the RA for the high conductance state with a value of 0.028 KΩμm^2 is of the same order of magnitude as the high conductance state of DB-FTJ (0.093 KΩμm^2). Overall, the DB-FTJ performs better than the SB-FTJ with 5.5 u.c. barrier thickness due to the much larger TER ratio.

The second SB-FTJ for comparison has a longer barrier by removing the metal layer from the DB-FTJ, with an aim to see whether the larger TER in the DB-FTJ can be restored by simply doubling the thickness of the single barrier. If it works, then the design will get much simpler, making the DB design also not necessary. The relaxed structures for the two polarization states of a SB-FTJ with BTO thickness of 11.5 u.c. are shown in Fig. 6c and the corresponding k-resovled transmissions are shown in Fig. 6d.

Similarly, the Ti-O displacement of the TiO$_2$ layer of ferroelectric barrier BTO [Supplementary Fig. 6a] and the electrostatic potential energy distribution of this system [Supplementary Fig. 6b] show the same characteristics as the SB-FTJ with BTO thickness of 5.5 u.c. and DB-FTJ. It is seen from the projected density of states that the CBM in the right region of the ferroelectric barrier BTO drops below the Fermi energy in the right polarization state, and this high conductance state is mainly contributed by d_{yz} and d_{xz} orbitals [Supplementary Fig. 7], which is consistent with the DB-FTJ discussed previously. As the thickness of the barrier increases, the conductance of the left polarization state [$1.510 \times 10^{-14}(2e^2h^{-1})$] and the right polarization state [$1.283 \times 10^{-10}(2e^2h^{-1})$] decreases greatly. Although there is still a big difference between the conductance of the two polarization states, with the TER ratio of $8.496 \times 10^5\%$, it is three orders of magnitude smaller than that of the DB-FTJ. Moreover, the RA of the high conductance state is 16.002 MΩμm^2, which is six orders of magnitude higher than the high conductance state of SB-FTJ with BTO thickness of 5.5 u.c. and
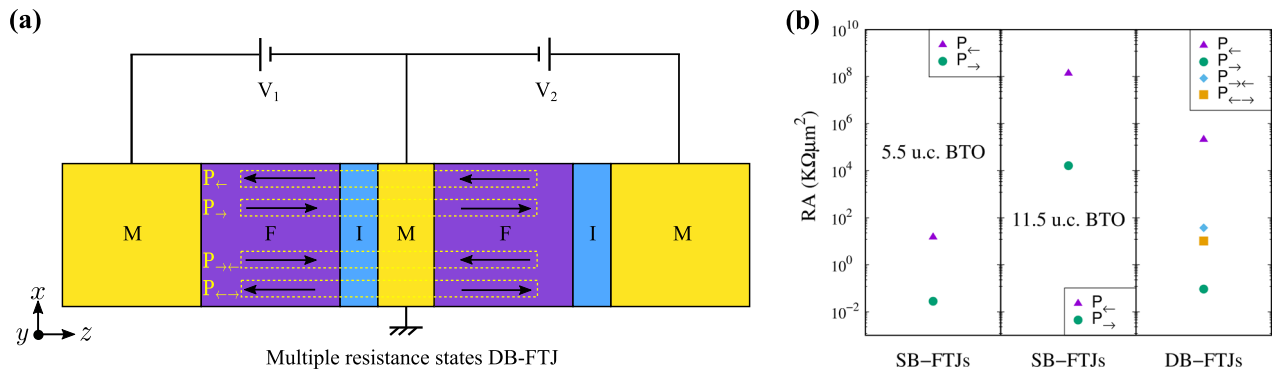
(a)

(b)

Fig. 7 Multiple resistance states DB-FTJ. a Schematic model of the multiple resistance states DB-FTJ, in which metal (M), ferroelectric (F), and interlayer (I) are, respectively, represented by yellow, purple, and blue rectangles. V_1, V_2 represent the bias used to control the direction of polarization of each single ferroelectric barrier. The arrows in the four yellow dotted boxes represent the four polarization states of the multiple resistance states DB-FTJ, and are represented by $P_{\leftarrow}$, $P_{\rightarrow}$, $P_{\rightarrow\leftarrow}$, and $P_{\leftarrow\rightarrow}$, respectively. **b** The RA of the SB-FTJs with BTO thickness of 5.5 u.c. and 11.5 u.c. and the multiple resistance states DB-FTJ in different polarization states.

the high conductance state of DB-FTJ. Thus, the difference between the two polarization states is not easy to detect since the currents in both states will be too small and beyond the detection limit[32].

We note that, in the DB-FTJs, the middle metallic layer is sandwiched between two insulating FE barriers, thus forming the quantum well (QW) states. The electron resonant tunneling through QW states would enhance the transmission. However, we should note that it will enhance the transmission for both polarization directions. This will not be the main factor of causing large difference in the transmissions between the two polarization states. The relation $T = T_a T_b$ will still hold. The main difference in the transmission in the two polarization states and the subsequent TER enhancement is mainly caused by the double barrier effect. As a matter of fact, the quantum states are just part of the DB-FTJ and the TER enhancement caused by the double barrier effect will always be significant. In addition, the defects and/or disorder may exist in ferroelectric tunnel junctions, which may have different effects on different polarization states, thus may enhance or weaken the TER ratios. By properly utilizing the defects and/or disorder, combined with the effect of the double barrier, we believe that a better TER ratio can be obtained in the DB-FTJs, which is well worth further investigation.

Multiple resistance states DB-FTJ

Finally, for the DB-FTJ, the structure characteristics of two single barriers in series can be used to further expand its function. We design a DB-FTJ model with multiple resistance states as shown in Fig. 7a. Bias V_1 and V_2 are used to control the polarization directions of the left and right ferroelectric barriers, respectively, so we can obtain the four polarization states as shown in the yellow dotted box in the figure. In the cases of two single ferroelectric barriers with both left and right polarization we have discussed above, it is confirmed that the ultra-low RA of the high conductance state and the TER ratio is at least three orders of magnitude larger than the SB-FTJs as compared above. The other two polarization states in Fig. 7a, i.e., with head-to-head and tail-to-tail polarization directions, are obtained by structural relaxation [Supplementary Fig. 8a, b]. The distribution of the electrostatic potential energy and PDOS of the head-to-head and tail-to-tail polarization states are shown in Supplementary Fig. 8c and Supplementary Fig. 9, respectively. Further analysis of the $k_\parallel$-resolved transmission of the head-to-head and tail-to-tail polarization states of the multiple resistance states DB-FTJ indicates that the transmission probability of the head-to-head polarization state near the $\bar{\Gamma}$ point in the 2DBZ is similar to that of the tail-to-tail polarization state [Supplementary Fig. 8d]. The conductance of the head-to-head polarization state is $5.492 \times 10^{-8} (2e^2h^{-1})$, and that of the tail-to-tail polarization state is $1.974 \times 10^{-7} (2e^2h^{-1})$. Correspondingly, the RA of the head-to-

head and tail-to-tail polarization state are 37.407 KΩμm² and 10.407 KΩμm², respectively. For comparison, we plotted the RA of different resistance states including the SB-FTJs and the multiple resistance states DB-FTJ [Fig. 7b]. It is seen that the multiple resistance states DB-FTJ realizes four resistance states in a large RA range, and there are obvious differences between these states. For the SB-FTJs with BTO thickness of 5.5 u.c. and 11.5 u.c., the TER magnitude is at least three orders of magnitude smaller than the TER of the left and right polarization states of the multiple resistance states DB-FTJ, and for the SB-FTJ with BTO thickness of 11.5 u.c., the RA of the high conductance state ($P_{\leftarrow}$) is clearly much larger than that in other FTJs.

In conclusion, we have designed and studied the Pt/BaTiO₃/LaAlO₃/Pt/BaTiO₃/LaAlO₃/Pt DB-FTJ based on a double barrier resonant tunneling model[36] by connecting two single barriers in series with nano-thick metal. For comparison, we have also studied the transport properties of Pt/BaTiO₃/LaAlO₃/Pt with a single ferroelectric barrier of different barrier thickness. For the DB-FTJ, we get ultra-low RA (0.093 KΩμm²) in the high conductance state and giant TER ratio (2.210×10^8%). In contrast, for the SB-FTJ with BTO thickness of 5.5 u.c. (or 11.5 u.c.), the TER ratio is about ~10⁴% (~10⁵%), which is at least three orders of magnitude smaller than that of the DB-FTJ, and the RA of the high conductance state of the SB-FTJ with BTO thickness of 11.5 u.c. is too large (16.002 MΩμm²). Therefore, the DB-FTJ will perform much better than the SB-FTJs in memory applications. In particular, by using bias to separately control the polarization direction of each single ferroelectric barrier in the DB-FTJ, we can extend the DB-FTJ from two resistive states to four resistive states to achieve multiple resistance states DB-FTJ, promising as multi-state memory devices. Thus the DB-FTJs have advantages over the SB-FTJs in many aspects for memory applications.

METHODS

For comparison, we study three devices, namely, the DB-FTJ [Pt/BTO(5.5 u.c.)/LAO(1 u.c.)/Pt/BTO(5.5 u.c.)/LAO(1 u.c.)/Pt], the SB-FTJ [Pt/BTO (5.5 u.c.)/LAO (1 u.c.)/Pt, and the SB-FTJ Pt/BTO (11.5 u.c.)/LAO (1 u.c.)/Pt]. Here a polar oxide barrier layer LAO is inserted at the right side of each single barrier since it has been demonstrated as a good interlayer in the M/F/I/M junctions for enhancing the TER performance[33]. The atomic plane terminations at each Pt/BTO interface are chosen such that the O atoms in the TiO₂ plane are right located at the top of the Pt atoms, which results in the most stable structure due to the strongest Coulomb attractive interaction between the Pt cations and O anions in contact. This Pt/BTO termination is also adopted in other studies on ferroelectric tunnel junctions[38,39]. For the Pt/LAO interface, a similar termination is chosen so that the O atoms of the AlO₂ plane are right at the top of Pt atoms. As for the atomic

terminations between BTO and LAO, since they both belong to the ABO_3 perovskite structure, naturally, the atomic planes between them should take an ...AO-BO_2-AO-BO_2... order, which is the one adopted in this work and other literatures[22,33,40].

The structure relaxation of these devices is performed with a $5 \times 5 \times 1$ k-sampling grid using the SIESTA package[41,42]. In the process of structural relaxation, following the routine in the literature[14,30,34], the xy plane lattice constant is fixed to the experimental lattice constant of tetragonal bulk BTO (namely, 3.991 Å)[13,39], while the atomic coordinates and z-direction lattice constant are fully optimized, which results in the electrodes undergoing a tetragonal phase distortion[13,39]. The maximum atomic force of atomic coordinate optimization is set to be less than 0.01 eV/Å. The Perdew–Burke–Ernzerhof (PBE) form of exchange-correlation potential under generalized gradient approximation (GGA)[43] and the double zeta combining polarization orbitals (DZP) are adopted throughout the work. The polarization direction of each single ferroelectric barrier BTO in the optimized system is obtained by pre-setting positive or negative Ti-O displacement. The BTO in the optimized tunnel junction has a tetragonal structure, and the value of c/a is larger than 1.0, indicating that polarization is present in the z-direction.

The transport properties are calculated by the Nanodcal package[44] which combines the DFT[45] and the nonequilibrium Green's functions (NEGF) method[46] specially for quantum transport study. The self-consistent calculations are performed using a $15 \times 15 \times 1$ k-point grid and the transmission coefficients are calculated with a 300×300 k-point grid of the transverse 2DBZ. The equilibrium conductance is calculated by

$$G = \frac{2e^2}{h} \sum_{\mathbf{k}_\parallel} T(E_F, \mathbf{k}_\parallel) \qquad (1)$$

where e is the electron charge, h is the Planck constant, and $T(E_F, \mathbf{k}_\parallel)$ is the transmission coefficient at the Fermi energy E_F and transverse Bloch wave vector $\mathbf{k}_\parallel = (k_x, k_y)$. The tunneling electro-resistance ratio is calculated by

$$TER = \frac{|G_\leftarrow - G_\rightarrow|}{\min(G_\leftarrow, G_\rightarrow)} \times 100\% \qquad (2)$$

to characterize the conductance difference between the left and right polarization states. Here, $G_\leftarrow$ and $G_\rightarrow$ are the equilibrium conductances of the left and right polarization states, respectively. Moreover, we integrate local density of states $n(\mathbf{r}, E)$ over the energy from $E_F - 0.1$ eV to E_F to obtain the real space charge density distribution of the system around the Fermi energy.

DATA AVAILABILITY
The atomic structure, electronic structure, and transport information involved in the device structure of the paper is presented in the main article and supplementary materials. More detailed raw data can be obtained by contacting the corresponding author.

CODE AVAILABILITY
The SIESTA code is freely available and used on its website. The Nanodcal code is charged.

REFERENCES

1. Junquera, J. & Ghosez, P. Critical thickness for ferroelectricity in perovskite ultrathin films. *Nature* **422**, 506–509 (2003).
2. Fong, D. D. et al. Ferroelectricity in ultrathin perovskite films. *Science* **304**, 1650–1653 (2004).
3. Sai, N., Kolpak, A. M. & Rappe, A. M. Ferroelectricity in ultrathin perovskite films. *Phys. Rev. B* **72**, 020101(R) (2005).
4. Tsymbal, E. Y. & Kohlstedt, H. Tunneling across a ferroelectric. *Science* **313**, 181–183 (2006).
5. Zhuravlev, M. Y., Sabirianov, R. F., Jaswal, S. S. & Tsymbal, E. Y. Giant electro-resistance in ferroelectric tunnel junctions. *Phys. Rev. Lett.* **94**, 246802 (2005).
6. Kohlstedt, H., Pertsev, N. A., Rodríguez Contreras, J. & Waser, R. Theoretical current-voltage characteristics of ferroelectric tunnel junctions. *Phys. Rev. B* **72**, 125341 (2005).
7. Chanthbouala, A. et al. Solid-state memories based on ferroelectric tunnel junctions. *Nat. Nanotechnol.* **7**, 101–104 (2012).
8. Kim, D. J. et al. Ferroelectric tunnel memristor. *Nano Lett.* **12**, 5697–5702 (2012).
9. Garcia, V. & Bibes, M. Ferroelectric tunnel junctions for information storage and processing. *Nat. Commun.* **5**, 4289 (2014).
10. Velev, J. P., Burton, J. D., Zhuravlev, M. Y. & Tsymbal, E. Y. Predictive modelling of ferroelectric tunnel junctions. *NPJ Comput. Mater.* **2**, 16009 (2016).
11. Boyn, S. et al. High-performance ferroelectric memory based on fully patterned tunnel junctions. *Appl. Phys. Lett.* **104**, 052909 (2014).
12. Abuwasib, M. et al. Scaling of electroresistance effect in fully integrated ferroelectric tunnel junctions. *Appl. Phys. Lett.* **108**, 152904 (2016).
13. Velev, J. P. et al. Magnetic tunnel junctions with ferroelectric barriers: prediction of four resistance states from first principles. *Nano Lett.* **9**, 427–432 (2009).
14. Burton, J. D. & Tsymbal, E. Y. Giant tunneling electroresistance effect driven by an electrically controlled spin valve at a complex oxide interface. *Phys. Rev. Lett.* **106**, 157203 (2011).
15. Wen, Z., Li, C., Wu, D., Li, A. & Ming, N. Ferroelectric-field-effect-enhanced electroresistance in metal/ferroelectric/semiconductor tunnel junctions. *Nat. Mater.* **12**, 617–621 (2013).
16. Jiang, L. et al. Tunneling electroresistance induced by interfacial phase transitions in ultrathin oxide heterostructures. *Nano Lett.* **13**, 5837–5843 (2013).
17. Yamada, H. et al. Giant electroresistance of super-tetragonal $BiFeO_3$-based ferroelectric tunnel junctions. *ACS Nano* **7**, 5385–5390 (2013).
18. Boyn, S. et al. Engineering ferroelectric tunnel junctions through potential profile shaping. *APL Mater.* **3**, 061101 (2015).
19. Liu, X., Burton, J. D. & Tsymbal, E. Y. Enhanced tunneling electroresistance in ferroelectric tunnel junctions due to the reversible metallization of the barrier. *Phys. Rev. Lett.* **116**, 197602 (2016).
20. Klyukin, K., Tao, L. L., Tsymbal, E. Y. & Alexandrov, V. Defect-assisted tunneling electroresistance in ferroelectric tunnel junctions. *Phys. Rev. Lett.* **121**, 056601 (2018).
21. Li, M., Tao, L. L., Velev, J. P. & Tsymbal, E. Y. Resonant tunneling across a ferroelectric domain wall. *Phys. Rev. B* **97**, 155121 (2018).
22. Li, M., Tao, L. L. & Tsymbal, E. Y. Domain-wall tunneling electroresistance effect. *Phys. Rev. Lett.* **123**, 266602 (2019).
23. Chen, L. et al. Enhancement of tunneling electroresistance by interfacial cation intermixing in ferroelectric tunnel junctions. *Appl. Surf. Sci.* **512**, 145707 (2020).
24. Su, Y. et al. Van der Waals multiferroic tunnel junctions. *Nano Lett.* **21**, 175–181 (2021).
25. Wang, J. & Li, Z. Y. Tunnel junctions with a ferroelectric-ferromagnetic composite barrier. *Appl. Phys. Lett.* **93**, 112501 (2008).
26. Zhuravlev, M. Y., Wang, Y., Maekawa, S. & Tsymbal, E. Y. Tunneling electroresistance in ferroelectric tunnel junctions with a composite barrier. *Appl. Phys. Lett.* **95**, 052902 (2009).
27. Wu, Y.-Z., Ju, S. & Li, Z.-Y. Effects of electrodes and space charges on the tunneling electroresistance in the ferroelectric tunnel junction with a $SrTiO_3$/$BaTiO_3$ composite barrier. *Appl. Phys. Lett.* **96**, 252905 (2010).
28. López-Encarnación, J. M., Burton, J. D., Tsymbal, E. Y. & Velev, J. P. Organic multiferroic tunnel junctions with ferroelectric poly(vinylidene fluoride) barriers. *Nano Lett.* **11**, 599–603 (2011).
29. Petraru, A., Soni, R. & Kohlstedt, H. Tunneling magnetoresistance and electroresistance properties of composite-barrier ferroelectric tunnel junctions. *Phys. Stat. Solid.* **6**, 138–140 (2012).
30. Yin, Y. W. et al. Enhanced tunnelling electroresistance effect due to a ferroelectrically induced phase transition at a magnetic complex oxide interface. *Nat. Mater.* **12**, 397–402 (2013).
31. Wu, Q. et al. Giant tunneling electroresistance induced by ferroelectrically switchable two-dimensional electron gas at nonpolar $BaTiO_3$/$SrTiO_3$ interface. *Phys. Rev. B* **94**, 155420 (2016).
32. Wang, L. et al. Overcoming the fundamental barrier thickness limits of ferroelectric tunnel junctions through $BaTiO_3$/$SrTiO_3$ composite barriers. *Nano Lett.* **16**, 3911–3918 (2016).
33. Yang, Q. et al. Ferroelectric tunnel junctions enhanced by a polar oxide barrier layer. *Nano Lett.* **19**, 7385–7393 (2019).
34. Jiang, L. N. et al. First-principles prediction of switchable metallic ferroelectricity in multiferroic tunnel junctions. *Phys. Rev. B* **99**, 224103 (2019).

35. Griffiths, D. *Introduction to Quantum Mechanics* (Pearson Prentice Hall, 2005).

36. Datta, S. *Electronic Transport in Mesoscopic Systems* (Cambridge University Press, 1995).

37. Hu, Y. & Stapleton, S. Sequential tunneling versus resonant tunneling in a double-barrier diode. *J. Appl. Phys.* **73**, 8633–8636 (1993).

38. Shen, L. et al. Systematic study of ferroelectric, interfacial, oxidative, and doping effects on conductance of $Pt/BaTiO_3/Pt$ ferroelectric tunnel junctions. *Phys. Rev. B* **85**, 064105 (2012).

39. Velev, J. P., Duan, C.-G., Belashchenko, K. D., Jaswal, S. S. & Tsymbal, E. Y. Effect of ferroelectricity on electron transport in $Pt/BaTiO_3/Pt$ tunnel junctions. *Phys. Rev. Lett.* **98**, 137201 (2007).

40. Tao, L. L. & Wang, J. Ferroelectricity and tunneling electroresistance effect driven by asymmetric polar interfaces in all-oxide ferroelectric tunnel junctions. *Appl. Phys. Lett.* **108**, 062903 (2016).

41. Sánchez-Portal, D., Ordejón, P., Artacho, E. & Soler, J. M. Density-functional method for very large systems with LCAO basis sets. *Int. J. Quantum Chem.* **65**, 453–461 (1997).

42. Soler, J. M. et al. The SIESTA method for ab initio order-N materials simulation. *J. Phys. Condens. Matter* **14**, 2745–2779 (2002).

43. Perdew, J. P., Burke, K. & Ernzerhof, M. Generalized gradient approximation made simple. *Phys. Rev. Lett.* **77**, 3865–3868 (1996).

44. Taylor, J., Guo, H. & Wang, J. Ab initio modeling of quantum transport properties of molecular electronic devices. *Phys. Rev. B* **63**, 245407 (2001).

45. Sholl, D. S. & Steckel, J. A. *Density Functional Theory: A Practical Introduction* (John Wiley & Sons, Inc., 2009).

46. Haug, H. & Jauho, A.-P. *Quantum Kinetics in Transport and Optics of Semiconductors* (Springer-Verlag, 1996).

47. Momma, K. & Izumi, F. VESTA: a three-dimensional visualization system for electronic and structural analysis. *J. Appl. Cryst.* **41**, 653–658 (2008).

AUTHOR CONTRIBUTIONS

W.X. designed and built the device model and carried out the first principles calculation. X.Z. guided the whole work. H.H., L.K., L.Z., and Z.Z. participated in the analysis and discussion of the data in this work.

COMPETING INTERESTS

The authors declare no competing interests.

ADDITIONAL INFORMATION

Supplementary information The online version contains supplementary material available at https://doi.org/10.1038/s41524-023-01101-9.

Correspondence and requests for materials should be addressed to Xiaohong Zheng or Lei Zhang.

Reprints and permission information is available at http://www.nature.com/reprints

Publisher's note Springer Nature remains neutral with regard to jurisdictional claims in published maps and institutional affiliations.